 FDMP, vol.11, no.1, pp.27-48, 2015

Acoustic Potential Generation under Acoustic Standing Waves Modeling using CFD Software.

C. S. Iorio[1] **and C. Perfetti**[1]

Abstract: In the past few years, modeling of the Acoustic Standing Waves (ASW) phenomena has become a topic of great interest due to its theoretical connections with particle/cells manipulation techniques, which represent important tools in the biotechnology field. The present paper proposes a model based on the use of moving wall boundary conditions coupled with a viscous compressible fluid in a square channel. This model successfully achieved the generation of ASWs in the square cross-section for several resonance frequencies; the corresponding acoustic potential for the fundamental resonant mode and several harmonics have also been calculated and are discussed here.

Keywords: Acoustic Standing Waves, Moving Walls, Computational Fluid Dynamics.

1 Introduction

In the past few years, modeling of the Acoustic Standing Waves (ASW) has been extensively studied for the better understanding of the particle /cells manipulation technique, that represents an important tool in the expanding of the biotechnology field. Focusing of particles or cells into the pressure node or anti-node positions, is often a crucial step for the further processing like separation [Tsutsui and Ho (2009)], observation, agglutination [Grundy, Moore, and Coakley (1994); Grundy, Bolek, Coakley, and Benes (1993); Hawkes and Coakley (1996)], concentration [Ravula, Branch, James, Townsend, Hill, Kaduchak, Ward, and Brener (2008); Neild, Oberti, Haake, and Dual (2006)]. Most of these studies were carried out close to the resonant frequency of the channel and for the fundamental mode. In this configuration, Townsend, Hill, Harris, and White (2004) have investigated particle paths for a separation application. On the other hand, higher harmonics have been seldom numerically investigated. Skafte-Pedersen and Bruus (2008) studied the second order velocity field for several modes in a 2 mm x 2 mm x 0.2 mm pool,

[1] Universite Libre de Bruxelles, Belgium.

while Bruus (2012) studied different acoustic modes by imposing a given velocity field at the boundaries; Townsend, Hill, Harris, and White (2006) and Townsend, Hill, Harris, and White (2004) investigated 3D enclosure mode using a 2D model with a transverse excitation in a rectangular channel. With the help of FemLab software, Neild, Oberti, Haake, and Dual (2006) managed to generate up to 12 lines of particles in a channel whose cross-section was 5mm x 0.2mm. However, the simple model was unable to eventually match experimental evidences. Modeling based on the finite elements [Wang and Dual (2009)] where the time-averaged acoustic forces act on rigid cylinders in both ideal and viscous fluids has been performed using the non-reflecting boundary conditions (perfectly matched layer (PML)).

The physical mechanism, describing the generation of the ASW by piezo actuator into a fluid medium is generally accepted as a mechanical deformation of the border. However, in most of the numerical models, the pressure or the velocity field are simply imposed through a reflective boundary condition, such as proposed by Townsend, Hill, Harris, and White (2006) and Glynne-Jones, Mishra, Boltryk, and Hill (2013) and are not calculated from the motion of the walls, as it should more physically be done. Besides, most of the models use a strong inviscid fluid assumption, resulting in a restricted description of the phenomena, as well as an important validity limitation.

In this paper, we present a model based on the use of the moving wall boundary conditions coupled with a viscous compressible fluid. Taking the advantage of the Fluent^{TM} software capabilities, the ASW is generated by the periodic deformation of the wall, modeled by a deforming mesh option controlled by a User Defined Function (UDF) [Iorio, Goncharova, and Kabov (2011)]. The compressibility of the fluid is introduced into the model by means of the state equation, linking the density to the pressure and the temperature fields. The standard patterns of the pressure field are successfully generated and the acoustic potential has been calculated in a square channel of 2 mm x 2 mm cross-section. Experimental investigations have been previously carried out by Iorio, Perfetti, Vancauwenberghe, and Dubois (2013).

2 Model Overview

Numerical modeling was an important step for the understanding and the foreseeing of the experimental device behavior and for the interpretation of the results in the post-processing phase. In the framework of this study, we used the commercial software Fluent^{TM} together with the mesh generator Gambit^{TM}. Fluent^{TM} belongs to the class of the full Navier-Stokes (NS) equations solvers. It includes several standard discretization schemes and physical models, for the implementation of applications-specific terms in both NS equations and boundary conditions, strongly

enhancing its numerical capability.

2.1 Geometry

The goal of the present model is to describe the pressure field generated by the acoustic standing waves. The geometry where the acoustic manipulation of particle is performed results in general in a flow channel of rectangular cross-section, where a piezo transducer is glued on one side and a reflector is glued on the opposite wall (Fig. 1). While the particles are flowing under a disperse distribution when an external field is not applied, they join an equilibrium position called a pressure node when an ASW is generated in the channel.

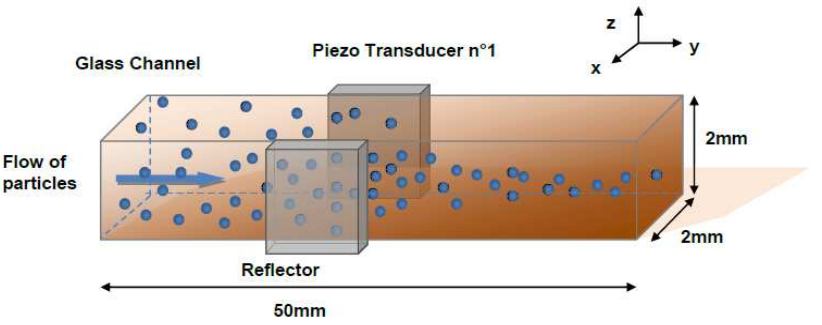

Figure 1: General scheme of the channel

Besides a transverse reflection of the wave by the reflector, the present model takes into account the non-planar characteristics of the acoustic wave by enabling lateral reflections. This feature is crucial in order to accurately generate the pressure field in the present model due its square geometry.

The 2D model under consideration is a cross-section of the square channel, orthogonal to the flow direction (See Fig. 2).

The left boundary of the channel corresponds to the transverse transducer that stands for the piezo actuation. Its velocity is described as U_T. The opposite wall corresponds to the transverse reflection boundary (U_{RT}), which is the main reflection mode. Upper and lower boundaries stand for the lateral reflection boundaries (U_{RL1} and U_{RL1}). This square geometry has been meshed with a total number of 68416 cells, their size ranging from 10μm to 2.5μm close to the wall, where a refinement is required to ensure a proper mesh deformation. Simulations have been performed on a Intel^{TM} quad-core 64bits, 16Gb of RAM. Based on this hardware

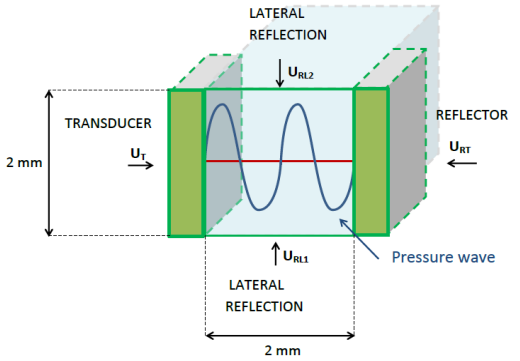

Figure 2: Geometry of the modeled cross-section.

configuration, the time required to achieve a meaningful simulation is roughly 1 day for a 2D unsteady laminar case. Modeled the acoustic wave generation and propagation is not a part of the standard, built-in, physical models of Fluent^{TM}. Basically an acoustic wave generation has been implemented by imposing a velocity condition at a boundary moving wall, coupled with the use of the Deforming Mesh option. The propagation of acoustic waves is calculated using a laminar model. In order to check for the validity of this assumption, turbulent model has also been tested and turbulent shear stresses evaluated. By considering that the solutions for the two models could be realistically super imposed and the turbulent stresses are negligible, the laminar model has been preferred for the sake of computational time. The general form of the continuity equation for a compressible and unsteady flow can be written as:

$$\frac{\partial \rho}{\partial t} + \nabla \cdot (\vec{v}\rho) = 0. \tag{1}$$

The conservation of momentum has the following form:

$$\frac{\partial}{\partial t}(\rho \vec{v}) + \nabla \cdot (\rho \vec{v}\vec{v}) = -\nabla p. \tag{2}$$

When the motion is not imposed to the boundaries, the no-slip condition is applied to the rigid walls. These equations Eq.(1) and Eq.(2) are closed by the boundary conditions described in the next paragraph.

2.2 Moving walls

The motion of the boundary is defined through a User Defined Function as a cosine function. The incident wave displacement could be calculated by integrating over

time the periodic boundary velocity U^i, where $i = T, RT, RL1, RL2$. U^i is applied orthogonally to the boundary, as described in Fig. 2. In the model, it is imposed this:

$$\begin{aligned} U_i^t &= A_i * \cos(-\frac{\pi}{2} + \frac{2\pi t}{\tau N}), \\ U_T &= U_i^t, \end{aligned} \tag{3}$$

$$\begin{aligned} U_{RT} &= U_i^t \quad \text{or} \quad U_{RT} = -U_i^t, \\ U_{RL1} &= 0 \quad \text{or} \quad U_{RL1} = U_T, \\ U_{RL2} &= 0 \quad \text{or} \quad U_{RL1} = U_{RT}. \end{aligned} \tag{4}$$

Here A_i is the amplitude of the signal applied to the boundary i, τ is the period of the signal, corresponding to the half-wavelength condition for the ASW generation and N is the number of the expected pressure nodes ($N = 1$ when a 1-node ASWis generated, $N = 2$ for a 2-node ASW and $N = 3$ when a 3-node ASW is generated in the channel).

An additional parity condition associated to the expected number of pressure nodes N in the channel. If N is an even number, $U_{RT}^t = U_T^t$, and if N is an odd number, $U_{RT}^t = -U_T^t$. The mesh deformation, generated by the displacement of the moving wall, is recovered by adjacent lateral walls that are set as deforming walls. The complete UDF, implemented in Fluent^{TM} is presented in Appendix A:.

2.3 Material properties

The material properties used in the described model are based on the water liquid properties, see Table 1. The compressibility of the fluid has been implemented thanks to the Equation of State of the water, where the density ρ is expressed as a function of the temperature T and the pressure P.

Table 1: Water liquid properties

Property	Symbol	Value	Unity (SI)
Dynamic Viscosity	η	0.001003	kg.m^{-1}.s^{-1}
Speed of sound	c	1507	m.s^{-1}
Specific Heat	C_P	4182	J.kg^{-1}.K^{-1}
Thermal conductivity	k	0.6	W.m^{-1}.K^{-1}
Density	ρ	User-defined	kg.m^{-3}

The density is calculated from the Equation of State developed by Chen, Fine, and Millero (1977) for water for 0°C $\leq T \leq$ 100°C and 0 bar $\leq P \leq$ 1000 bar and

explained in detailed in Appendix B:.

$$\rho = \frac{1}{V}, \quad V = V_0 - \frac{V_0 P}{K_0 + AP + BP^2}. \tag{5}$$

Here V_0 and V are the specific volumes at $P = 0$ bar and P respectively, K_0 is the secant bulk modulus at $P = 0$ bar, A and B are the temperature-dependent parameters. The speed of sound is expressed as:

$$c^2 = \left[\frac{\partial P}{\partial \rho}\right]_S. \tag{6}$$

Here the subscript S indicates the isoentropicity. The speed of the sound has been calculated from Eq. (5). However, its variations are negligible and setting a constant value do not modify significantly the results.

2.4 Acoustic radiation force

The acoustic radiation force results in the superposition of the incoming and the scattered wave. When the superposition of the traveling waves leads to an acoustic standing wave, the radiation pressure is unbalanced everywhere except from the pressure nodes so that the suspended particles move towards their equilibrium position. Nodes location can be thus assimilate to stable mechanical equilibrium points from the acoustic point of view. Acoustic forces are conservatives, i.e., they act as a field depending only on the position and, as a consequence they can be expressed in terms of a gradient of a potential field. The acoustic potential derived by Gor'kov (1962) for an arbitrary acoustic field on a spherical particle of radius r can be expressed as:

$$\langle U \rangle = \frac{4\pi r^3}{3}\left(f_1 \langle E_{pot} \rangle - f_2 \frac{3}{2} \langle E_{kin} \rangle\right), \tag{7}$$

Here E_{pot} is the time-averaged potential energy, E_{kin} is the time-averaged kinetic energy and the material contrast factors f_1 and f_2 are defined as:

$$f_1 = 1 - \frac{\rho_m c_m^2}{\rho_p c_p^2} \tag{8}$$

$$f_2 = \frac{2(\rho_p - \rho_m)}{2\rho_p + \rho_m} \tag{9}$$

$$\langle E_{pot} \rangle = \frac{\langle p^2 \rangle}{2\rho_m c_m^2} \tag{10}$$

$$\langle E_{kin} \rangle = \frac{\rho_m \langle v^2 \rangle}{2} \tag{11}$$

$$\Phi = f_1 + \frac{3}{2} f_2. \tag{12}$$

Here ρ is the density of the fluid in the absence of the perturbation, c is the sound velocity, the subscript m refers to the medium properties, while the subscript p refers to the particle properties, $\langle p^2 \rangle$ is the time-averaged span pressure and $\langle v^2 \rangle$ is the time-averaged span velocity due to the acoustic wave. Eq. 7 shows that the force experienced by a particle is a function of the cube of its radius r^3 and the material contrast factors f_1 and f_2 between the particle and the fluid. When the acoustic force is integrated in the propagation direction, the acoustic factor Φ can be defined as a linear combination of the material contrast factors f_1 and f_2, and is commonly used for the prediction of the particle behavior under acoustic standing wave. The acoustic contrast factor is a dimensionless number used for the description of the acoustic behavior between two materials, based on their relative density ρ and the speed of the sound c. The material properties that have been incorporated in the present model are displayed in Table. 2.

2.5 Acoustic potential

The static pressure and the velocity field can give only a representation of the system at a specific time t while the mean pressure and the mean velocity remain equal to zero due to the exact superposition of the waves under the ASW condition. However, the acoustic radiation force experimented by the particles under the ASW depends on the second order terms of the perturbation of the pressure and the velocity. These terms are taken into account in the so-called time-averaged values of the pressure and the velocity. The time-averaged values of the pressure and the velocity are calculated in Fluent^{TM}, using the Root-Mean-Square (RMS) of the pressure - P_{RMS} - and the velocity - V_{RMS} - fields that could be defined as:

$$\langle P^2 \rangle = \frac{1}{T} \int_0^T P(t)^2 dt = P_{RMS}^2 \tag{13}$$

$$\langle V^2 \rangle = \frac{1}{T} \int_0^T V(t)^2 dt = V_{RMS}^2. \tag{14}$$

Here T represents the global calculation time, and $P(t)$ and $V(t)$ are the instantaneous values of the static pressure and the velocity field. At each pressure node, the RMS velocity field exhibits a maximum, while the RMS pressure field exhibits a minimum. These fields are representative of the acoustic effect and will be used to define the acoustic potential and the radiation force, that are responsible for the particle migration. As stated above, an acoustic potential is also a function

of the particle radius. To facilitate the further comparisons between experiments and numerical results, we have normalized the acoustic potential $\langle U_{rad} \rangle$ against the particle volume.

$$\langle U_{rad} \rangle = \frac{3}{4\pi r^3} \langle U \rangle . \tag{15}$$

For the sake of completeness, the acoustic contrast factors in Eq.(12) have been evaluated for a typical microparticle suspension Iorio, Perfetti, Vancauwenberghe, and Dubois (2013). Medium is set as the water, while particles are considered as being microsphere of the polyethylene. These objects are often used as biomimetic particles in biological experiments. Acoustic potential is calculated in Fluent^{TM}

Table 2: Acoustic Contrast factors

Material	Property& Symbol	Value in (USI)
Particle : Polyethylene	Density ρ_p	998.2 kg.m^{-1}.s^{-1}
Particle : Polyethylene	Speed of sound c_p	2430 m.s^{-1}
Medium: Water	Density ρ_m	User-defined kg.m^{-3}
Medium: Water	Speed of sound c_m	1507 m.s^{-1}

using a Custom Field Function, where the time-averaged kinetic and potential energies are implemented according the Eq. (7).

3 Numerical results

3.1 Acoustic Standing Wave generation

The ASW phenomena corresponds to the constructive superposition of incident and scattered waves in the channel. The static pressure along the width of the channel for a 1-node, 2-node and 3-node ASW is shown respectively in Fig. 3, Fig. 4 and Fig. 5.

Several time intervals t are displayed in these figures: $t = n\tau$, $t = n\tau + \frac{1}{4}\tau$, $t = n\tau + \frac{1}{2}\tau$ and $t = n\tau + \frac{3}{4}\tau$ where τ corresponds to the period of the acoustic wave and n is the number of computed periods. When $t = n\tau$ and $t = n\tau + \frac{1}{2}\tau$, the acoustic pressure reaches a zero value (small perturbation comes from the differences in the mean of the computed time-steps), while the maximum values are displayed at $t = n\tau + \frac{1}{4}\tau$ and $t = n\tau + \frac{3}{4}\tau$.

3.2 Acoustic wave propagation

One of the interesting results obtained with our model was the possibility to follow the propagation of the acoustic wave through the medium in the transient phase,

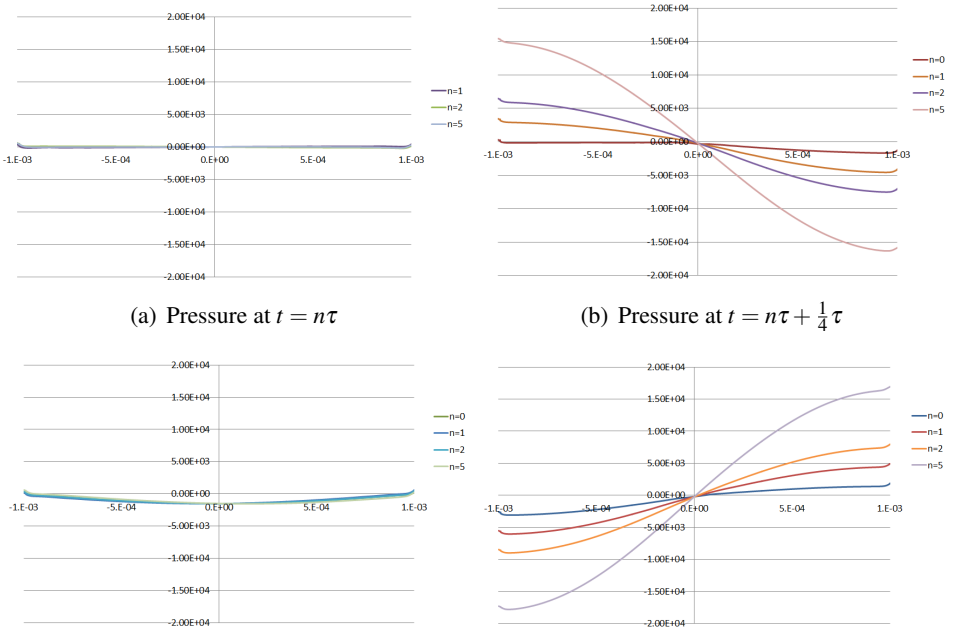

(a) Pressure at $t = n\tau$

(b) Pressure at $t = n\tau + \frac{1}{4}\tau$

(c) Pressure at $t = n\tau + \frac{1}{2}\tau$

(d) Pressure at $t = n\tau + \frac{3}{4}\tau$

Figure 3: The instantaneous pressure evolution of the 1-node wave period (f=400KHz); Y axis: Pressure (Pa) and X axis: The channel width (m). The origin of the x-axis $x = 0$ is set at the center of the channel cross-section, and the left and right wall of the channel are located at $x = -1$ and $x = +1$ respectively; the geometrical position of the node is located at $x = 0$mm.

preceding the establishment of a standing wave inside the channel. This analysis allowed to check whether the waves generated by the motion of the walls are not attenuated by the numerical viscosity of the chosen discretization schemes and correctly propagated with a velocity, corresponding to the speed of the sound in the medium. A scheme of the wave propagation is presented in Fig. 2.

The initial transient phase of the ASW generation is followed by the plotting of the static pressure for 10 successive time intervals of the first period τ of the acoustic wave propagation. The generation of a 1-node acoustic wave is presented in Fig. 6 (red lines). The genration of a 2-node ASW is shown in Fig. 7 (green lines), and the generation of a 3-node ASW is show in Fig. 8. In these figures, the instantaneous static pressure is presented by a plain line, while the previous steps are shown by the dashed lines.

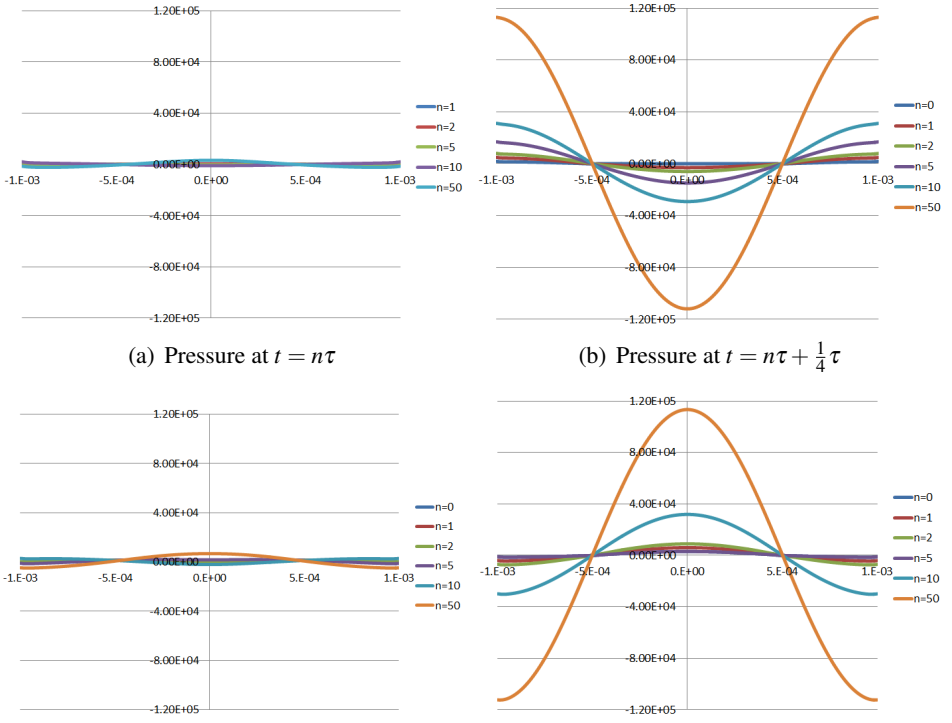

(a) Pressure at $t = n\tau$

(b) Pressure at $t = n\tau + \frac{1}{4}\tau$

(c) Pressure at $t = n\tau + \frac{1}{2}\tau$

(d) Pressure at $t = n\tau + \frac{3}{4}\tau$

Figure 4: The instantaneous pressure evolution of the 2-node wave period (f=800KHz); Y axis: Pressure (Pa) and X axis: The channel width (m). The origin of the x-axis $x = 0$ is set at the center of the channel cross-section, and the left and right wall of the channel are located at $x = -1$ and $x = +1$ respectively; the geometrical positions of the 2 nodes are located at $x = -0.5$ mm and $x = 0.5$mm.

3.3 Transverse and orthogonal actuation

The patterns of the particles positions in the cross section of the channel that have been experimentally observed by Iorio, Perfetti, Vancauwenberghe, and Dubois (2013) presented a peculiar distribution in form of spots or ribbons. To our knowledge, the formation of this matrix-like structure has never been reported in the literature. To understand better how these structures could arise, we have investigated the hypothesis of a multiple reflection of the incident wave, both on the lateral wall of the channel but also on the orthogonal walls of the channel. The corresponding formation of spots could then be due to the preponderantly scattering role of the orthogonal side walls of the channel that would reflect the incident wave

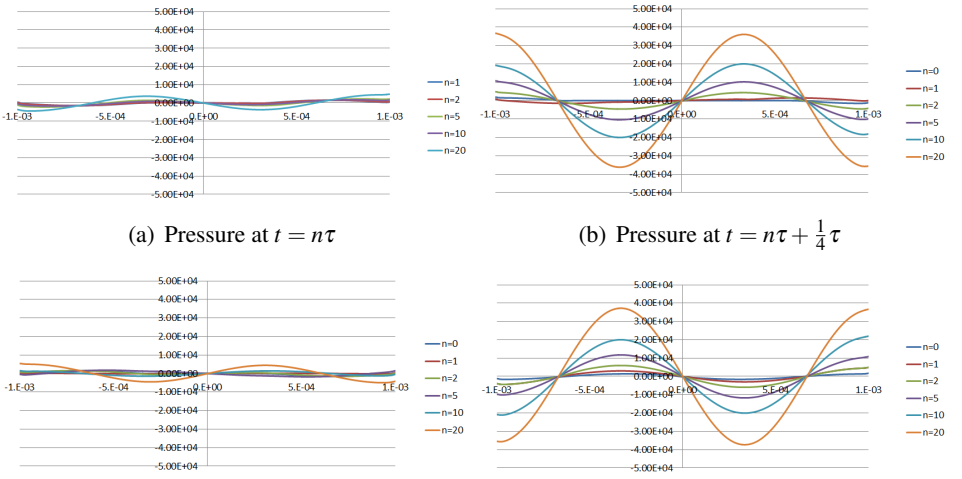

(a) Pressure at $t = n\tau$

(b) Pressure at $t = n\tau + \frac{1}{4}\tau$

(c) Pressure at $t = n\tau + \frac{1}{2}\tau$

(d) Pressure at $t = n\tau + \frac{3}{4}\tau$

Figure 5: The instantaneous pressure evolution of the 3-node wave period (f=1.2MHz); Y axis: Pressure (Pa) and X axis: The channel width (m). The origin of the x-axis $x = 0$ is set at the center of the channel cross-section, and the left and right wall of the channel are located at $x = -1$ and $x = +1$ respectively; the geometrical positions of the 3 nodes are located at $x = -0.67$ mm, $x = 0$ mm and $x = 0.67$ mm.

in the same way that the transverse reflector. This hypothesis has been tested by the implementation a 2D model that enables the independent motion of the 4 outer boundary walls. The patterns generated by the conjugate action of the transverse and the orthogonal actuation modes could be then investigated as shown in Fig. 2. The velocity motion has been set to the orthogonal walls similarly to the previous transverse actuation, as defined in paragraph 2.2.

3.3.1 Acoustic potential

As described previously, the acoustic potential is the superposition of the time-averaged kinetic energy and the time-averaged potential energy (Eq. (7)). Fig. 9 displays the potential energy, the kinetic energy and the normalized by radius acoustic potential resulting from the transverse and the orthogonal actuation with the same magnitude, in the case of a 3-node acoustic standing wave. The minimum values for the kinetic energy are located in 9 spots, that are symmetrically distributed into the cross-section. The minimum values for the potential energy form a network with a 45 degree shift.

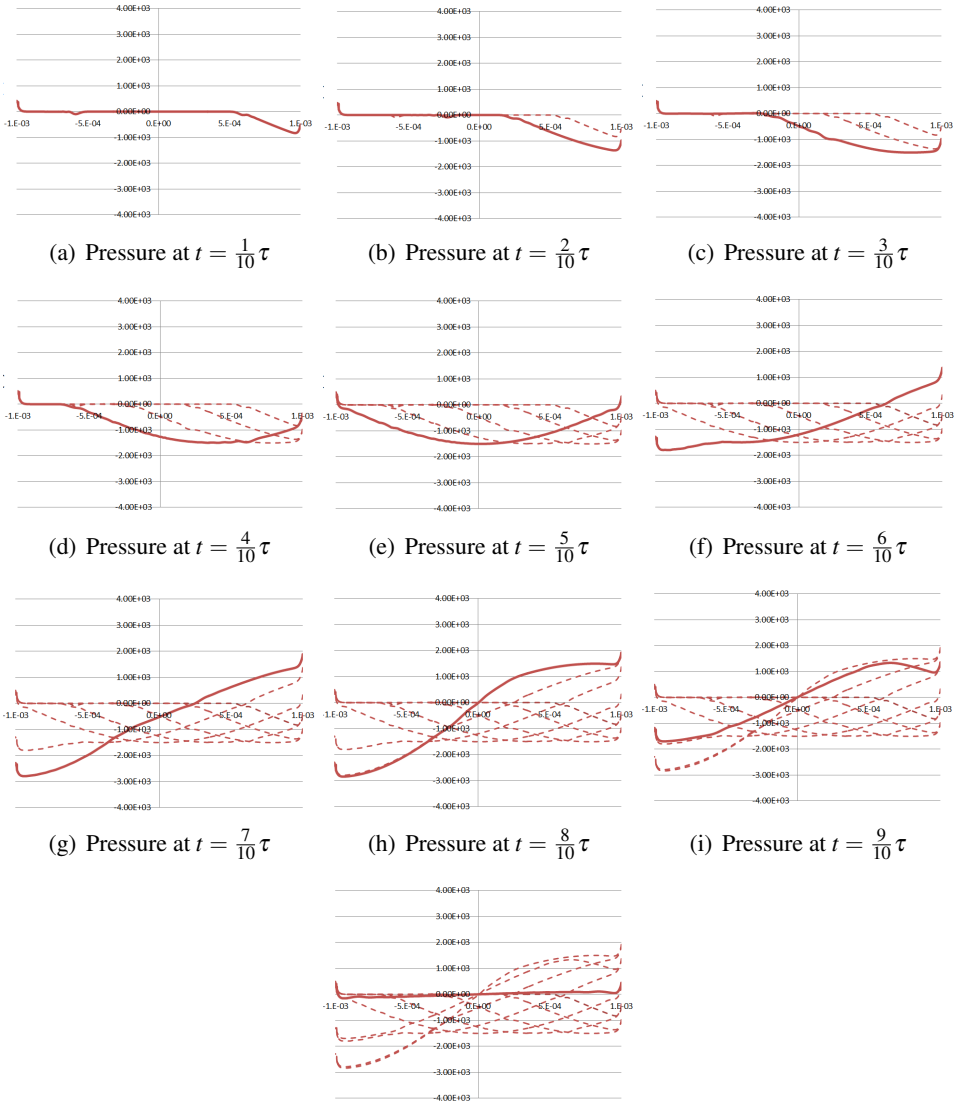

(a) Pressure at $t = \frac{1}{10}\tau$ (b) Pressure at $t = \frac{2}{10}\tau$ (c) Pressure at $t = \frac{3}{10}\tau$

(d) Pressure at $t = \frac{4}{10}\tau$ (e) Pressure at $t = \frac{5}{10}\tau$ (f) Pressure at $t = \frac{6}{10}\tau$

(g) Pressure at $t = \frac{7}{10}\tau$ (h) Pressure at $t = \frac{8}{10}\tau$ (i) Pressure at $t = \frac{9}{10}\tau$

(j) Pressure at $t = \tau$

Figure 6: Generation of 1-node ASW in the channel (f=400kHz); Y axis: Pressure (Pa) and X axis: The channel width (m).

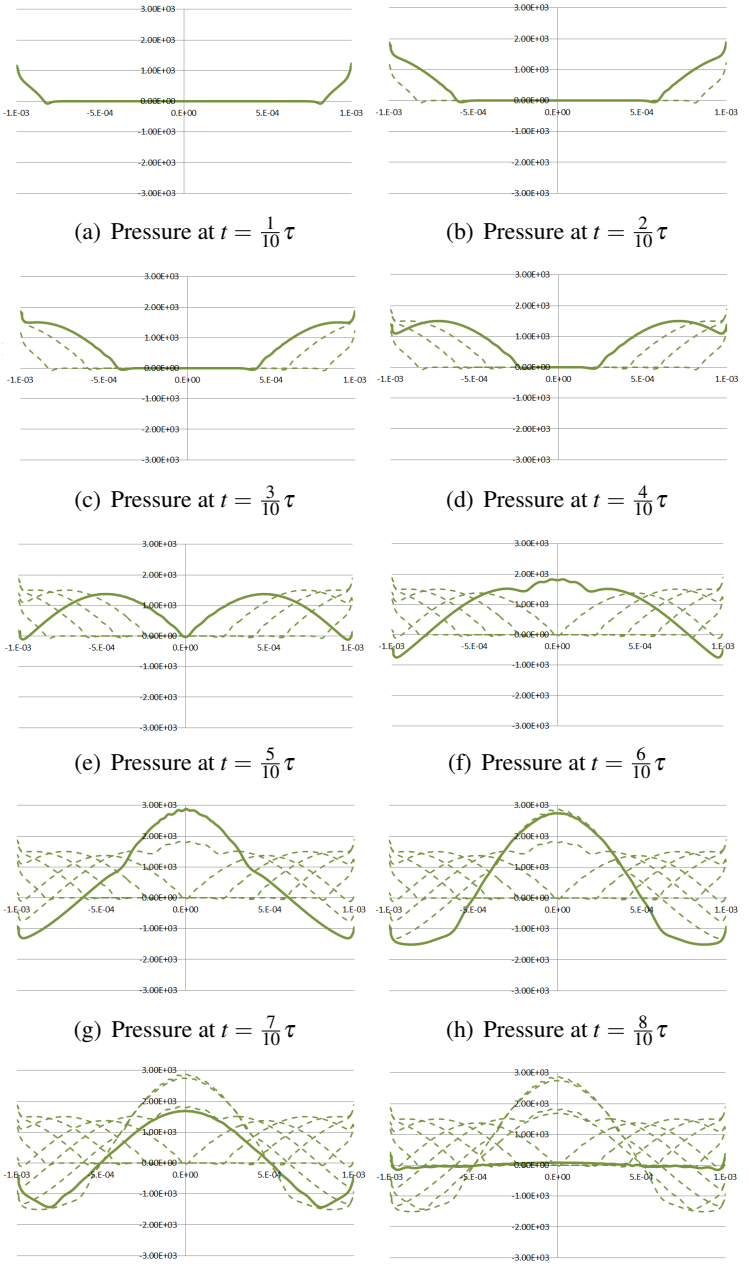

(a) Pressure at $t = \frac{1}{10}\tau$ (b) Pressure at $t = \frac{2}{10}\tau$

(c) Pressure at $t = \frac{3}{10}\tau$ (d) Pressure at $t = \frac{4}{10}\tau$

(e) Pressure at $t = \frac{5}{10}\tau$ (f) Pressure at $t = \frac{6}{10}\tau$

(g) Pressure at $t = \frac{7}{10}\tau$ (h) Pressure at $t = \frac{8}{10}\tau$

(i) Pressure at $t = \frac{9}{10}\tau$ (j) Pressure at $t = \tau$

Figure 7: Generation of a 2-node ASW in the channel (f=800kHz); Y axis: Pressure (Pa) and X axis: The channel width (m).

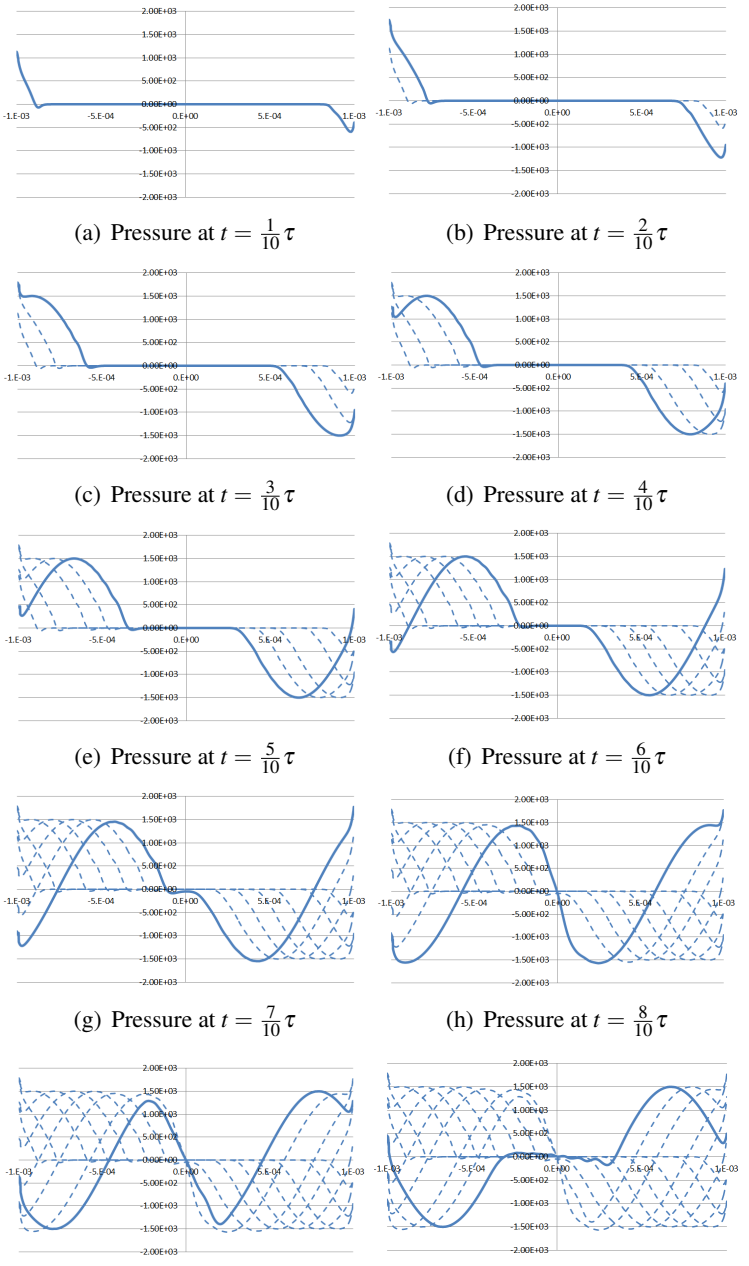

(a) Pressure at $t = \frac{1}{10}\tau$ (b) Pressure at $t = \frac{2}{10}\tau$

(c) Pressure at $t = \frac{3}{10}\tau$ (d) Pressure at $t = \frac{4}{10}\tau$

(e) Pressure at $t = \frac{5}{10}\tau$ (f) Pressure at $t = \frac{6}{10}\tau$

(g) Pressure at $t = \frac{7}{10}\tau$ (h) Pressure at $t = \frac{8}{10}\tau$

(i) Pressure at $t = \frac{9}{10}\tau$ (j) Pressure at $t = \tau$

Figure 8: Generation of a 3-node ASW in the channel (f=1.2MHz); Y axis: Pressure (Pa) and X axis: The channel width (m).

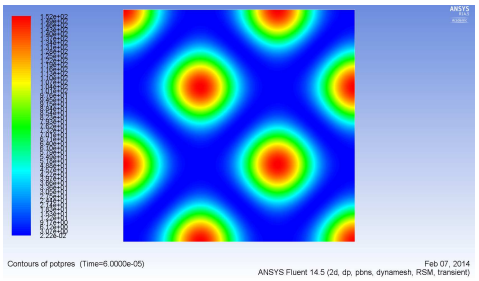

(a) Potential Energy (3-node ASW; $t = 60\mu$s)

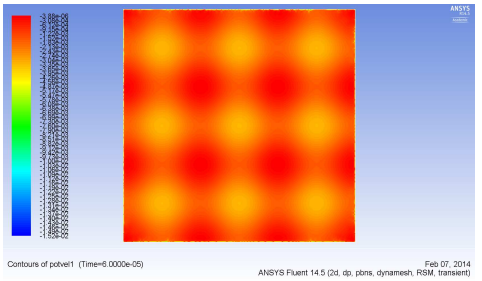

(b) Kinetic Energy (3-node ASW; $t = 60\mu$s)

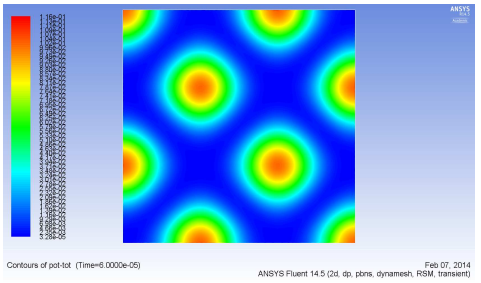

(c) Acoustic Potential (3-node ASW; $t = 60\mu$s)

Figure 9: An acoustic potential resulting from the superposition of the Kinetic Energy and the Potential Energy (3-node ASW; $t = 60\mu$s, f=1.2MHz).

The ASW generation over time is displayed in Fig. 10 under the transverse and the orthogonal actuation with the same amplitude. The minimum values for acoustic potential generated using the transverse and the orthogonal model, present weavy lines that would provide a better representation of the experimental patterns with respect to the case where the transverse actuation is only imposed.

This result confirms the assumption of a crucial role, played by the orthogonal wall reflections in the dispersion of particles under the ASW in a square cross-section channel. Still, having imposed the same amplitude for the incident and the orthogonally scattered wave, a symmetrical distribution of the acoustic potential is obtained.

3.3.2 Impact of an asymmetrical actuation

Fig. 11 displays different amplitude ratios of the transverse and the orthogonal actuation for the same calculation time. From $A_{RL} = 0$ (Fig.11(a)) to $A_{RL} = A_T$ (Fig.11(d)), the acoustic potential exhibits an increase of its weavy-like behavior.

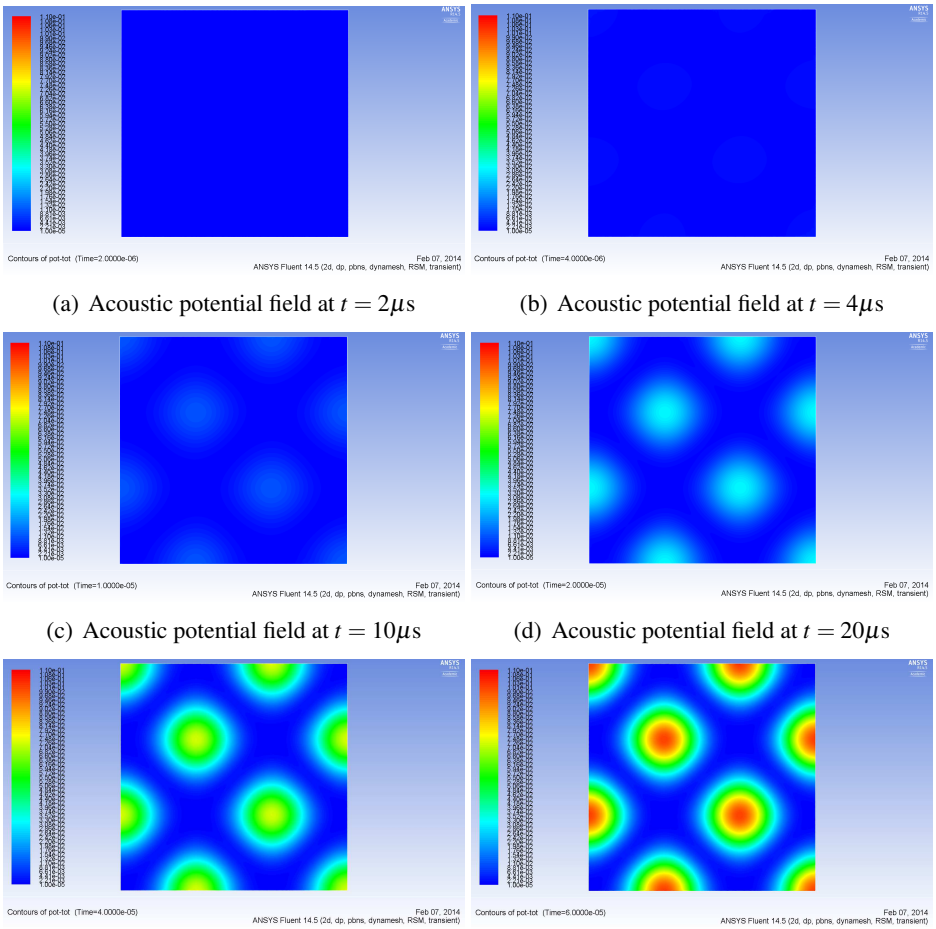

(a) Acoustic potential field at $t = 2\mu$s

(b) Acoustic potential field at $t = 4\mu$s

(c) Acoustic potential field at $t = 10\mu$s

(d) Acoustic potential field at $t = 20\mu$s

(e) Acoustic potential field at $t = 40\mu$s

(f) Acoustic potential field at $t = 60\mu$s

Figure 10: 3-node ASW generation in the cross-section of the channel under the transverse and the orthogonal actuation (f=1.2MHz).

4 Conclusion

A numerical model for the determination of the acoustic forces and the potentials in a fluidic channel of a square cross-section has been developed. In the frame of this paper, a numerical model has been implemented to investigate the multiple reflection of the incident wave, not only on the transverse opposite wall of the channel, but also on the orthogonal walls of the channel. These lateral reflections of the acoustic signal are due to the non-planar wave. The model was supposed to reproduce the real motion of the walls as induced by the vibrations of the piezoelectric

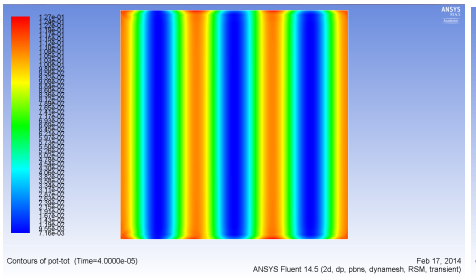

(a) Acoustic potential field with asymmetrical stimulation amplitude $A_{RL} = 0$

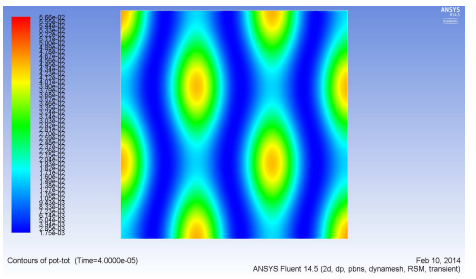

(b) Acoustic potential field with asymmetrical stimulation amplitude $A_{RL} = \frac{1}{4}A_T$

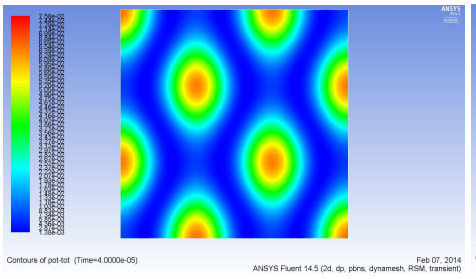

(c) Acoustic potential field with asymmetrical stimulation amplitude $A_{RL} = \frac{1}{2}A_T$

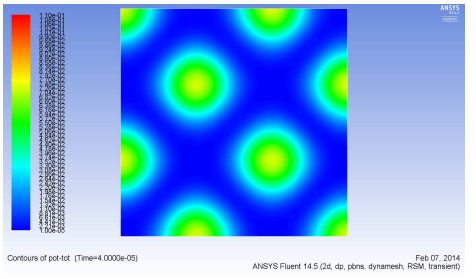

(d) Acoustic potential field with symmetrical stimulation amplitude $A_{RL} = A_T$

Figure 11: Comparison of the normalized by the radius acoustic potential under a 3-node ASW in the cross-section of the channel for different amplitude ratios of the transverse and the orthogonal actuation ($t = 40\mu$s, f=1.2MHz)).

elements, in order to be able to autonomously generate the acoustic standing waves and the related potential.

The generation of a non-attenuated, standing wave has been the first important validation of the model. The generation of the ASW under a transverse and orthogonal actuation has been reported. The resulting acoustic potential field has been displayed for several resonance modes. Eventually, the investigation of an asymmetrical stimulation using a different amplitude for the orthogonal and the transverse actuation has been presented.

References

Bruus, H. (2012): Acoustofluidics 2: Perturbation theory and ultrasound resonance modes. *Lab Chip*, vol. 12, pp. 20–28.

Chen, C.-T.; Fine, R. A.; Millero, F. J. (1977): The equation of state of pure

water determined from sound speeds. *The Journal of Chemical Physics*, vol. 66, no. 5, pp. 2142–2144.

Glynne-Jones, P.; Mishra, P. P.; Boltryk, R. J.; Hill, M. (2013): Efficient finite element modeling of radiation forces on elastic particles of arbitrary size and geometry. *The Journal of the Acoustical Society of America*, vol. 133, no. 4, pp. 1885–1893.

Gor'kov, L. P. (1962): On the forces acting on a small particle in an acoustical field in an ideal fluid. *Soviet Physics Doklady*, vol. 6, pp. 773.

Grundy, M.; Bolek, W.; Coakley, W.; Benes, E. (1993): Rapid agglutination testing in an ultrasonic standing wave. *J. Immunol Methods.*, vol. 165, pp. 47–57.

Grundy, M.; Moore, K.; Coakley, W. (1994): Increased sensitivity of diagnostic latex agglutination tests in an ultrasonic standing wave field. *J. Immunol Methods.*, vol. 176 (2), pp. 169–77.

Hawkes, J. J.; Coakley, W. (1996): A continuous flow ultrasonic cell-filtering method. *Enzyme and Microbial Technology*, vol. 19, no. 1, pp. 57 – 62.

Iorio, C.; Perfetti, C.; Vancauwenberghe, V.; Dubois, F. (2013): 3d focusing of microparticles by acoustic standing waves in a flow through channel. *Proceedings - ICNMM- Sapporo (JP)*.

Iorio, C. S.; Goncharova, O. N.; Kabov, O. A. (2011): Heat and mass transfer control by evaporative thermal patterning of thin liquid layers. *Computational Thermal Sciences: An International Journal*, vol. 3, no. 4, pp. 333–342.

Neild, A.; Oberti, S.; Haake, A.; Dual, J. (2006): Finite element modeling of a microparticle manipulator. *Ultrasonics*, vol. 44, Supplement, pp. 455 – 460. Proceedings of Ultrasonics International (UI'05) and World Congress on Ultrasonics (WCU).

Ravula, S. K.; Branch, D. W.; James, C. D.; Townsend, R. J.; Hill, M.; Kaduchak, G.; Ward, M.; Brener, I. (2008): A microfluidic system combining acoustic and dielectrophoretic particle preconcentration and focusing. *Sensors and Actuators B: Chemical*, vol. 130, no. 2, pp. 645 – 652.

Skafte-Pedersen, P.; Bruus, H. (2008): Acoustofluidic simulations: Ultrasound handling of liquids and particles in microfluidic systems. *Proceedings - ICNMM*.

Townsend, R.; Hill, M.; Harris, N.; White, N. (2004): Modelling of particle paths passing through an ultrasonic standing wave. *Ultrasonics*, vol. 42, pp. 319–324. Proceedings of Ultrasonics International 2003.

Townsend, R.; Hill, M.; Harris, N.; White, N. (2006): Investigation of two-dimensional acoustic resonant modes in a particle separator. *Ultrasonics*, vol. 44, pp. e467–e471.

Tsutsui, H.; Ho, C.-M. (2009): Cell separation by non-inertial force fields in microfluidic systems. *Mechanics Research Communications*, vol. 36, no. 1, pp. 92 – 103. Recent Advances in Microfluidics.

Wang, J.; Dual, J. (2009): Numerical simulations for the time-averaged acoustic forces acting on rigid cylinders in ideal and viscous fluids. *Journal of Physics A: Mathematical and Theoretical*, vol. 42, no. 28, pp. 285502.

Appendix A: User Defined Function - Wall motion

```
#include "udf.h"
#include "dpm.h"
#include "stdio.h"
#include "models.h"
```

```
#define OM 4.73438e6
#define PI 3.1415926535
#define TM 2.65428E^-06 %for a 2mm wide channel and with a speed of sound of
1507m.s^-1
#define N 3 %number of selected nodes

#define RMS(mean_accum, rms_accum, n, nsq)
sqrt(/*1/(N_TIME)**/fabs(rms_accum/n-SQR(mean_accum)/nsq))
```

V_Up

```
#DEFINE_CG_MOTION(translation_U, dt, vel, omega, time, dtime)
{
Thread *t;
face_t f;
NV_S(omega, =, 0.0);
t = DT_THREAD(dt);
begin_f_loop (f,t) {
if(N==1||N==3||N==5) if N is an even number, L and R are in phase
{vel[1]=A0/2*cos(-M_PI/2+2*_PI*time/(TM/N));}
```

```
else
{
```

FIRST CYCLE

```
vel[1]=-A0/2*cos(-M_PI/2+2*M_PI*time/(TM/N));}
end_f_loop (f,thread)
}
}
```

V_Down

```
DEFINE_CG_MOTION(translation_D, dt, vel, omega, time, dtime)
{
Thread *t;
face_t f;
NV_S(omega, =, 0.0);
t = DT_THREAD(dt);
begin_f_loop (f,t) {
vel[1]=A0/2*cos(-M_PI/2+2*M_PI*time/(TM/N));
end_f_loop (f,thread)
}
}
```

V_Right

```
DEFINE_CG_MOTION(translation_R, dt, vel, omega, time, dtime)
{
Thread *t;
face_t f;
NV_S(omega, =, 0.0);
t = DT_THREAD(dt);
begin_f_loop (f,t)
{
if(time<=TM/(2))
```

```
{
vel[0]=0;
}
else
{
if(N==1||N==3||N==5)
{
vel[0]=A0*cos(-M_PI/2+2*M_PI*(time-TM/(2))/(TM/N));
}
else
{
vel[0]=-A0*cos(-M_PI/2+2*M_PI*(time-TM/(2))/(TM/N));
}
}
end_f_loop (f,thread)
}
}
```

V_Left

```
DEFINE_CG_MOTION(translation_L, dt, vel, omega, time, dtime)
{
Thread *t;
face_t f;
NV_S(omega, =, 0.0);
t = DT_THREAD(dt);
begin_f_loop (f,t)
{
if(time<=TM/(2))
{
vel[0]=0;
}
else
{
vel[0]=A0*cos(-M_PI/2+2*M_PI*(time-TM/(2))/(TM/N));
}
end_f_loop (f,thread)
}
```

```
}
```

Appendix B: User Defined Function - Material Properties

```
#include "udf.h"
#include "dpm.h"
#include "stdio.h"
#include "models.h"
#define A0 0.001 [K]
```

```
DEFINE_PROPERTY(rhoA,c,t)
{
real dens,K0,V0,A,B,V;
real temp = C_T(c,t)-273.15;
real pres = C_P(c,t);
real presat;
K0=-4E-05*temp*temp*temp*temp + 0.0122*temp*temp*temp - 2.2883*temp*temp
+ 148.09*temp + 19652;
V0=4E-10*temp*temp*temp*temp - 7E-08*temp*temp*temp + 8E-06*temp*temp
- 6E-05*temp + 1.0002;
A=9E-10*temp*temp*temp*temp - 8E-07*temp*temp*temp + 0.0001*temp*temp
+ 0.0005*temp + 3.2614;
B=4E-12*temp*temp*temp*temp - 1E-09*temp*temp*temp + 9E-08*temp*temp
- 6E-06*temp + 7E-05;
presat= pres/101325;
V=V0-V0*presat/(K0+A*presat+B*presat*presat);
dens=(1/V)*1000;
return dens;
}
```